Reversible Wrinkling Surfaces for Enhanced Grip on Wet/Dry Conditions

Jooyeon Shin, Jong-Gu Lee, Gunhee Lee, Peter V. Pikhitsa, Sang Moon Kim, Mansoo Choi,* and Yong Whan Choi*

Cite This: ACS Appl. Mater. Interfaces 2022, 14, 48311−48320 | Read Online

ACCESS | Metrics & More | Article Recommendations | Supporting Information

ABSTRACT: Friction is important in material design for robotic systems that need to perform tasks regardless of environmental changes. Generally, robotic systems lose their friction in wet environments and fail to accomplish their tasks. Despite the significance of maintaining friction in dry and wet environments, it is still challenging. Here, we report a smart switching surface, which helps to complete missions in both wet and dry environments. Inspired by the reversible wrinkling mechanism of a human finger, the surface reversibly generates and removes wrinkles to adapt to both environments using volume-changing characteristics of the Nafion film. The switchable surfaces with manipulated wrinkle morphologies via patterns of diverse densities, sizes, and shapes induce a relationship between the wrinkle morphologies and friction: wrinkles on denser and smaller hexagonal patterns generate six times more friction than non-switching flat surfaces in wet environments and a similar amount of friction to the flat surfaces in dry environments. In addition, the wrinkle morphologies according to the patterns are predicted through numerical simulation, which is in good agreement with experimental results. This work presents potential applications in robotic systems that are required to perform in and out of water and paves the way for further understanding of wrinkling dynamics, manipulation, and evolutionary function in skin.

KEYWORDS: reversible wrinkling surface, friction, surface pattern, wrinkle, telephone cord buckling, biomimetics
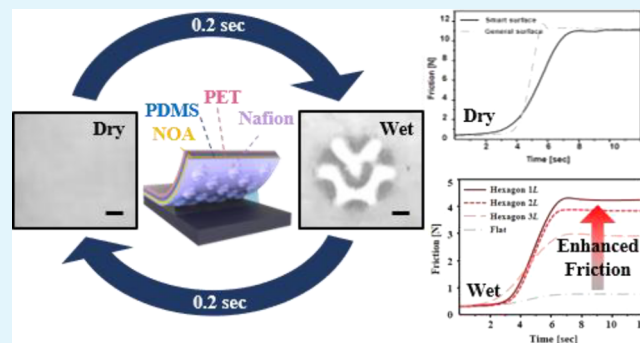
1. INTRODUCTION

An attachment system has recently gained attention in interdisciplinary scientific research due to its applicability to various fields such as grippers,[1−5] mobile robots,[6−10] and medical devices.[11−13] The adhesive and frictional systems, especially, play an important role in the performance of robots in activities such as climbing, jumping, and grasping. As moving in unpredictable environments and grasping vulnerable and irregularly shaped objects are challenging, various methods have been proposed including biomimic structures,[1,4,5,9] thermally responsive shape-memory actuators,[3,14,15] and pressure-driven actuators.[16,17] One of the biomimic approaches, dry attachment systems inspired by gecko's hairy attachment pads, has been extensively studied.[1,18,19] The gecko attachment system is now identified to operate on the principle that dense hairs enhance both adhesive and frictional forces by contact splitting. Another approach is an origami system in a vacuum-driven gripper inspired by a magic ball, whose shape allows us to grip objects of various forms and shapes with a force that is 10 times greater than a non-magic ball-shaped gripper.[2] Another mobile robot that operates on the principle of origami can climb over obstacles on a slope with wheels inspired by an umbrella.[7]

However, all these methods only work for dry attachment and have limitations for use in wet environments. In spite of its significance in machines that are required to operate on rainy days or submerge in water, wet attachment has not been studied sufficiently. Among the research studies on wet attachment, there are two representative studies. One way to enhance attachment in wet environments is to prevent slipping on uneven surfaces. A good example can be found in tree and torrent frogs.[20−23] They move freely in wet environments without sliding with the aid of their toe-pads. Their surface consists of hexagonal microstructures (10−15 μm) and micro-sized channels (~1 μm). The channels are formed by the separation of epithelial cells that are hexagonal in shape. The mechanism of their attachment in wet conditions has not been fully understood, but a draining effect through the channels has been suggested as the key. Another well-known example is
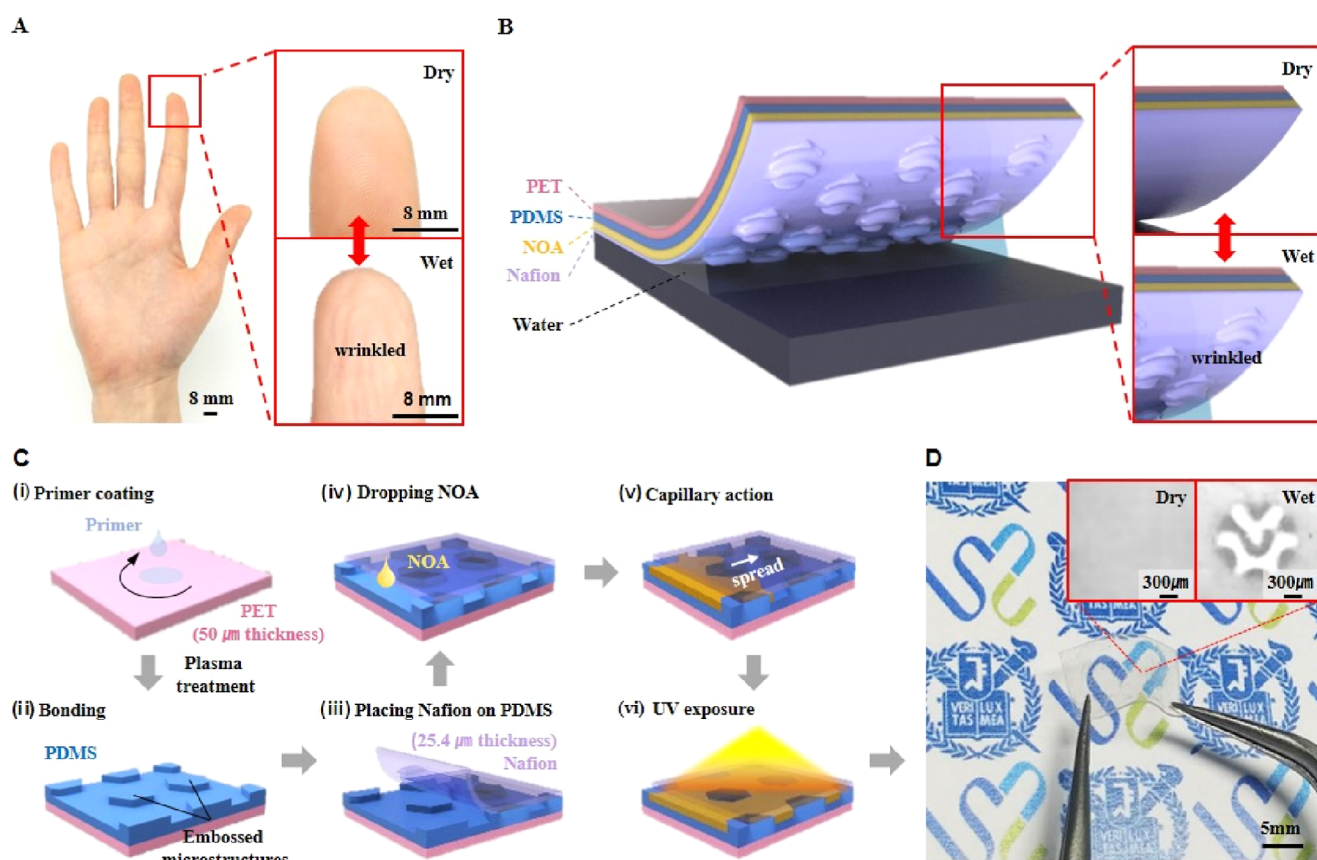
Figure 1. Illustrations and images of reversible wrinkles inspired by a human finger. (A) Human finger that wrinkles in wet conditions and returns to its flat state in dry conditions. (B) Schematic illustration of the human finger-inspired structure (PET/PDMS/NOA/Nafion) that forms reversible wrinkles. (C) Schematic diagram of the fabrication process with a capillary action. (D) Photographic images of the completely fabricated structure (hexagon 3L, 50%) that is flexible and transparent. Permission to use Seoul National University logos was granted by Seoul National University.

automobile tires.[24] Running on dry roads in particular, racing cars use smooth tires that generate a large frictional force due to their wide contact area. On a wet road, however, the smooth tires are likely to slip due to the hydroplaning phenomenon that occurs when a layer of water is created between the tires and the surface of the road. Therefore, tires with threads are used because the drainage networks that they create strengthen the friction. Although these thread and channel systems improve friction in wet conditions, the protrusive structures in these systems decrease the contact area and this reduction leads to a significant decrease in frictional force in dry conditions.[25] Another disadvantage is that their surfaces need to be manually replaced to maintain the largest frictional force depending on the surfaces. Therefore, there is a demand for a smart system that can automatically switch its surface between smooth and bumpy states.

Our concept of the smart switching system is inspired by a human finger in wet conditions. When it is exposed to water for a period of time, wrinkles are generated. This wrinkling mechanism was commonly believed to be the result of osmotic reactions.[26,27] However, this assumption fails to explain the case of denervated fingers that do not form wrinkles when exposed to water.[28] This inexplicable phenomenon indicates that the sympathetic nervous system could be involved in the wrinkling process.[29] Although the effect of wrinkles is still controversial, there is a view that the wrinkling response

regulated by the nerve is a functional adaptation in order to help fingers catch the specimen better in the water.

To date, wrinkling patterns have been well studied for taking advantage of their unique properties such as friction,[30−32] sensitivity,[33,34] and other physical properties.[35] Some attempts have been made to control wrinkling patterns and to explore the effect of wrinkling patterns on friction.[30−32,36−38] Sun et al.[30] created wrinkling patterns on the metal film/soft polymer substrate bilayer system and controlled surface friction by simply controlling thickness and film materials. Furthermore, Yuan et al.[31] reported that surface friction could be controlled by substrate curvature and film thickness, which induces different wrinkling morphologies on the spherical metal film/soft polymer substrate system. Although all these studies provided a new understanding of the frictional behavior of wrinkled surfaces, it is still a challenge to create functional surfaces with wrinkling patterns.

Many reversible wrinkling systems have also been reported. For instance, Tianjiao[39] fabricated light-driven dynamic wrinkling surfaces on a single bilayer system with a pigment-containing substrate. As thermal expansion induced by the photothermal effect affected the wrinkles, the optical properties, such as the scattering of light and the interference color of the system, were controlled via the wavelength of light. Kai[40] also reported reversible wrinkling surfaces via introducing stress on an oxidation film−substrate bilayer system. These solvent-responsive wrinkles were controlled by the modulus
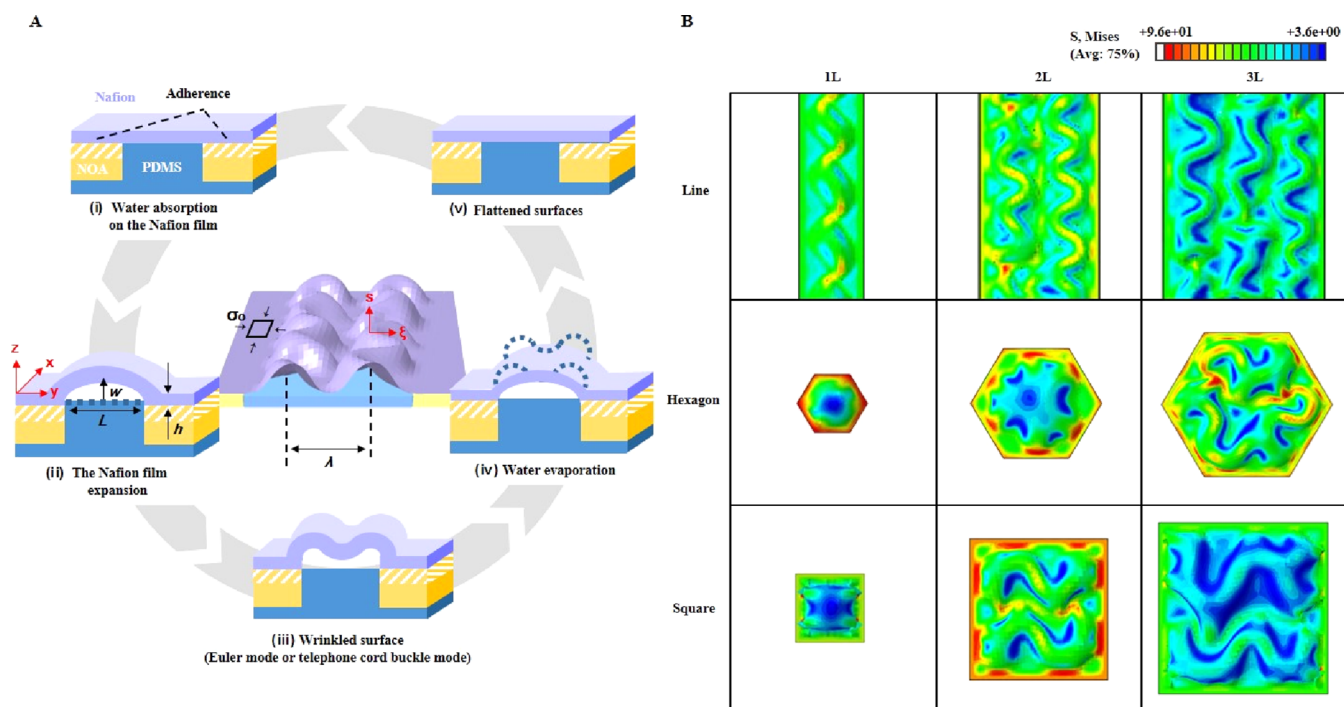
Figure 2. Numerical analysis of wrinkles formed on various patterns. (A) Proposed mechanism of wrinkle formation and disappearance in the sample. For the straight-sided buckle mode (Euler mode), the ratio of the biaxial compressive stress (σ_0) to the critical biaxial compressive stress (σ_c) is less than the specific ratio, and for the telephone cord buckle mode, σ_0/σ_c is greater than the specific ratio. (B) Numerical simulation results of three-dimensional wrinkle morphologies developed on patterns of various sizes (1L, 2L, and 3L) and shapes (line, hexagon, and square).

and thickness of the oxidation layer through the ultraviolet−ozone treatment time. These two methods introduced dynamic stress-driven wrinkles on the all-in-one bilayer system without the use of any batteries and successfully harnessed their stimulus-responsive optical characteristics for smart displays. However, there is a limit to the applications of devices that require improved grip such as long response times, large temperature dependence, and uncontrolled wrinkle morphologies; therefore, more research is needed.

Here, we report a novel strategy to generate a large frictional force in both dry and wet conditions, modeled analogously to the reversible wrinkles of a human finger. Our smart switching surface system forms telephone cord-buckled wrinkles in wet environments and returns to its originally flat surface in dry environments quickly. This unique function was feasible due to the special property of a Nafion film whose volume changes with wet or dry surroundings and interface adhesion. On the surface of the film, wrinkles were formed differently according to patterns of various densities, sizes, and shapes as the geometries of the patterns determined wrinkle morphologies with specific boundary conditions and biaxial compressive stress. To understand the dynamic morphological change of wrinkles deeply, we studied numerical analysis and the relation between a geometrical characteristic of the wrinkle and frictional force. On the basis of the research, we investigated morphology conditions that could be appropriate for our smart switching surface system, producing the largest friction. Finally, we applied the sample with the best conditions to the feet of a walking robot to confirm whether it can climb dry and wet slopes. We also compared gripping performance with a commercial gripper surface and our smart switching surface through experiments of picking up a dry or wet egg. From

these, we demonstrated the high applicability of our smart switching system that can be utilized in various fields.

2. RESULTS AND DISCUSSION

2.1. Reversible Wrinkling Surfaces. As seen in Figure 1A, wrinkles are formed when the fingers are submerged in water for a certain period of time and disappear when dried. Since this phenomenon is reversible, wrinkled and unwrinkled surfaces are repeatedly observed depending on the environment. Based on this feature, a schematic illustration of the human finger-inspired reversible wrinkling system is shown in Figure 1B. Similar to human fingers, its flat surfaces become wrinkled in wet conditions. Reversibly, its bumpy surfaces return to its original, flat ones in dry conditions. This replicable system maintains large frictional forces in both dry and wet environments. This is because the contact areas are maximized by eliminating wrinkles in dry conditions, while hydroplaning is prevented through wrinkles in wet conditions. This layer-by-layer structure is composed of a polyethylene terephthalate (PET) film, polydimethylsiloxane (PDMS) mold, Norland optical adhesives (NOA), and a Nafion film. Nafion, a commercially available copolymer, consists of a hydrophobic polytetrafluoroethylene (PTFE) backbone and perfluoroalkyl ether (PFA) side chains terminated by a hydrophilic sulfonic acid ionic group, which restructures their arrangement and forms micelles when the hydrophilic group absorbs water (Figure S1).[41−43] This is the mechanism of how a Nafion membrane swells in wet conditions. This volume-changing characteristic made the Nafion film perfectly imitate water-responsive skin wrinkling. In this work, the morphology of wrinkles was controlled by micro-patterns of PDMS molds. Under such control, the wrinkles are anchored by the pattern features through well-defined and fixed boundary conditions,
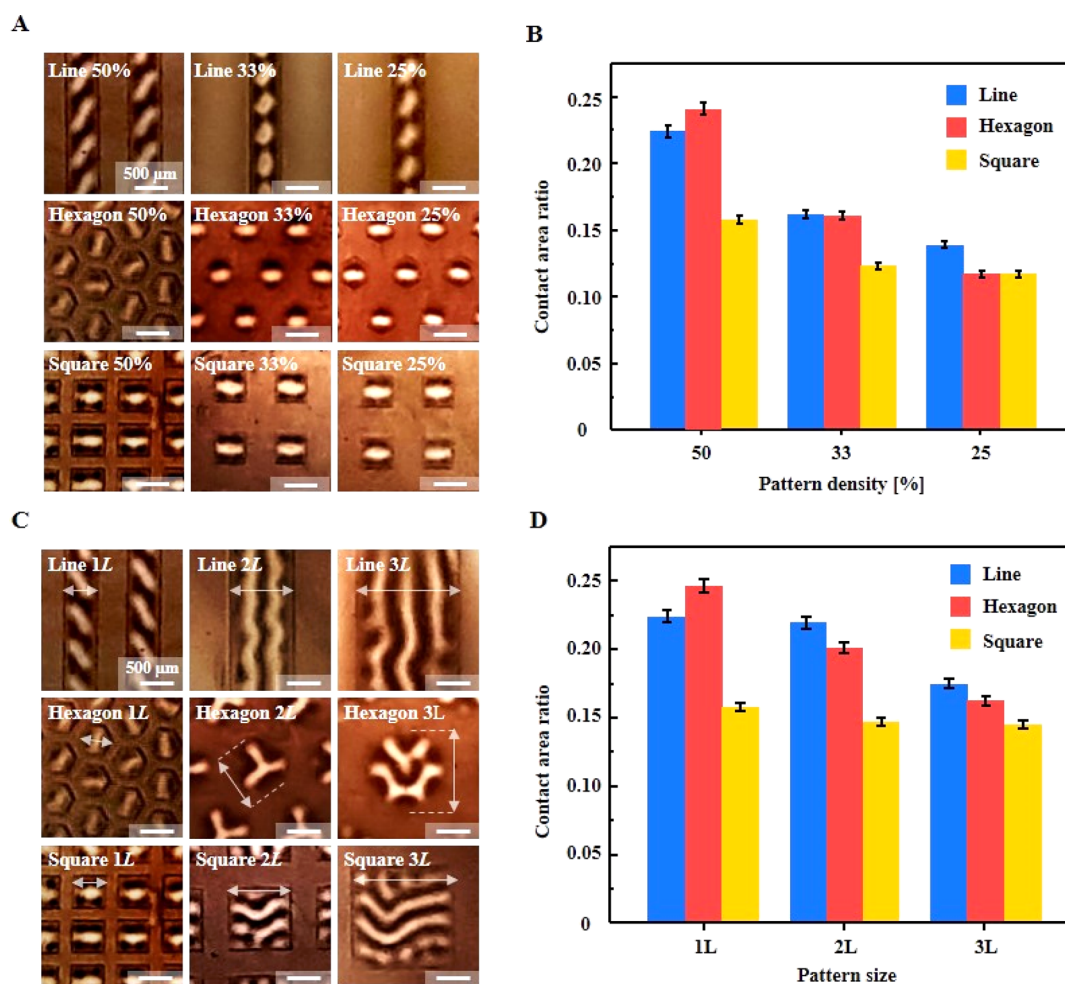
Figure 3. Wrinkles formed in various patterns. (A) Optical microscopic images of wrinkles developed on varied pattern shapes (line, hexagon, and square) and pattern densities (percentages of the patterned area over the total area of 50, 33, and 25%). All samples have the same pattern size (1*L*). (B) Static wrinkled area ratios of three pattern shapes (line, hexagon, and square) and three different pattern densities (50, 33, and 25%) (*n* = 5). (C) Optical microscopic images of wrinkles formed in a variety of shapes (line, hexagon, and square) and pattern sizes (1*L*, 2*L*, and 3*L*). The pattern density is the same in all samples (50%). (D) Average wrinkled area ratio of the three pattern shapes (line, hexagon, and square) and three pattern sizes (1*L*, 2*L*, and 3*L*) (*n* = 5).

which allows us to understand the relation between geometrical characteristics of the wrinkles and frictional force.

Details of the fabrication method are shown in Figure 1C. PDMS molds were attached to a flexible and primer-treated PET film (50 μm thickness) by plasma bonding. Next, a Nafion film (25.4 μm thickness) was put on the top of the molds. By capillary action, a UV curable polymer (NOA) was spread out that fulfilled the space between the patterns. Then, the NOA polymer between the patterns was bonded to the Nafion film by the UV curing process. In the area with patterns, on the other hand, the Nafion was simply placed on the PDMS patterns, where it could generate wrinkles in wet conditions. The sample completed in this way was transparent and flexible (Figure 1D).

2.2. Numerical Study of the Wrinkling Mechanism. When the sample was submerged in water, wrinkles were generated through the mechanism of wrinkling dynamics (Figure 2A). Following thin-plate theory based on the plane-stress assumption, the strain energy of a thin film is reduced and expressed into in-plane stretching and out-of-plane bending energy separately. Generally, stretching and bending energy scales are $E_s \cong Ehl^2$ and $E_b \cong Eh^3$, respectively, which

are functions of film thickness h, characteristic side-length l, and Young's modulus E. Considering that the thickness of Nafion film is much thinner compared to its characteristic side-length ($h/l \ll 1$), its in-plane stretching deformation takes more energy than out-of-plane bending deformation in terms of total strain energy. Thus, under compressive stress, a thin film is willing to be bent and adapted to a cylindrical shape.

Beyond the expectation that the Nafion film would be wrinkled in a cylindrical shape, the wrinkling phenomenon of the Nafion–PDMS bilayer showed a non-linear behavior under compressive stress. When the Nafion–PDMS bilayer is submerged in water, the Nafion film tends to swell in all directions because of its volume changing characteristic in water. If there is no specific interfacial boundary condition, it will be uniformly swelled on the patterned PDMS without a wrinkled shape. However, a portion of the Nafion film is strongly attached to the NOA polymer, which restricts the bending and stretching deformations of the Nafion film on the patterned PDMS substrate. Thus, out-of-plane bending and in-plane stretching energies are accumulated and compete with each other to minimize the total strain energy. Due to the effect of geometric boundary conditions induced by PDMS

patterns, the corresponding compressive stress and stretching energy are non-uniformly accumulated in the specimen. As a result, local bending deformation initiates at a certain point, propagates non-linearly, and then becomes wrinkled (Figure 2Ai−iii). In dry environments, as the water on the surface is removed and the water absorbed by the Nafion film evaporates, the bending and stretching energies applied to the Nafion film are released. As a result, the wrinkles disappear, and the surface returns to being flat (Figure 2Aiv,v).

Based on the wrinkling mechanism, finite element method (FEM)-simulation was performed to study the shape of wrinkles. The mechanical factors used in the FEM-based numerical analysis are shown in Tables S1, S2. The results in Figure 2B are similar to the previously reported buckling shapes of the thin film, which are subjected to biaxial compressive stress, σ_o, and adhered weakly to a rigid substrate.[44] In the earlier work, the buckling shapes were also divided into straight-sided buckle modes (Euler mode) and telephone cord buckle modes, representatively. For estimation of conditions determining buckling morphology, the non-dimensional stress ratio was introduced as (σ_0/σ_c), where σ_c states critical stress for the Euler buckle mode of a long plate clamped along its edges ($\pm L/2$)[45]

$$\sigma_c = \frac{\pi^2}{12} \frac{E}{1-\nu^2} \left(\frac{t}{L}\right)^2 \tag{1}$$

Under a specific stress ratio (σ_0/σ_c), buckling morphology was observed only in the Euler buckle mode. On the other hand, above the specific stress ratio (σ_0/σ_c), the telephone cord buckle mode appeared.[44] The stress ratio σ_0/σ_c can be changed not only by the averaged biaxial compressive stress σ_0 but also by the increase in the width of the line pattern because the critical stress σ_c is proportional to the square of the ratio of the width L and film thickness t. Thus, the stress ratio σ_0/σ_c increases as the width of the line pattern increases. As a result, below a specific width, that is, below the specific stress ratio, the Euler mode appears. Contrarily, above a specific width, that is, above the specific stress ratio, the telephone cord buckle mode appears. Similarly, the increase in the hexagon and square pattern size also induces the reduction of the ratio of the characteristic width to thickness (t/L) and the increment of the equivalent stress ratio σ_0/σ_c, corresponding to each pattern shape. In this paper, the pattern size is defined as the width of the line pattern, the diameter of the circumscribed circle in the hexagonal pattern, and the length of the square pattern. The unit size of $1L$ represents 500 μm. As the pattern size increased, the Euler mode-like buckling shape was converted to the telephone cord-like buckling shape. Moreover, with the change in pattern shape, compressive stress and stretching energy are non-uniformly accumulated as mentioned above. Thus, the initial propagation and intermediate branch points of the buckling mode (Euler mode and telephone cord mode) became different. As a result, the final wrinkle morphologies showed a much different configuration depending on the initial shape and size of patterns, which induced geometric boundary conditions. To identify the mechanism in more detail, transient numerical analysis of the wrinkle-generation process with the change in the biaxial compressive stress was conducted, and the results are shown in Figure S2 extracted from Movie S1.

2.3. Morphological Study of Wrinkles. According to the above studies, wrinkles could be controlled through the geometric properties of a unit-pattern on Nafion. First, we harnessed three different pattern densities (percentages of the patterned area divided by the total area, 50, 33, and 25%) and pattern shapes (line, hexagon, and square) to the same size, $1L$. Regardless of the pattern density, all patterns induced similar morphologies of wrinkles (Figure 3A). The average wavelength of each sample is shown in Table S3. The developed wrinkles generated different contact areas, one of the important factors in friction, according to the various geometric properties of the patterns. The contact area refers to the area where the sample is in contact with the tested surface when wrinkling occurs, and the method for measuring the contact area is provided in Figure S3. As a common method for contact area measurement, the ink method[46] uses a printed area, whereas our method observes an area where the light is transmitted. In our method, 2% aqueous solution of polystyrene (PS) microparticles was dropped on a slide glass, each of which was then covered with the samples. Then, these samples were observed through a microscope with a weight of 200 g placed on top. While the micro-particle aqueous solution does not transmit light clearly, only the contact area is observed to be bright. As the results show in Figure 3B, the measured contact area is almost proportional to the pattern density. Despite the same pattern density, the contact area was quite different according to pattern shapes. The reason was that wrinkle morphology depended on the shape of the pattern, and the detailed analysis will be provided in the following sections.

Next, wrinkles were manipulated by the other geometric properties of patterns in three different sizes ($1L$, $2L$, and $3L$) and shapes (line, hexagon, and square) with the same pattern density (50%). The patterns of various sizes and shapes induced different wrinkles (Figures 3C, S4−S6), of which the average wavelengths and amplitudes are also provided in Tables S3, S4, respectively. The wavelength and amplitude were formed with a constant ratio of the amplitude over the wavelength, 0.02 ± 0.004 (mean ± s.d., n = 9). It is well known that the wavelength of the wrinkles does not depend on the size of the pattern in the case of strong coupling between the film and the substrate.[47] The wavelength is proportional to the film thickness and the square root of the ratio of the Young's modulus of the film and the substrate. On the contrary, when the film only weakly interacts with the underlying substrate or is freely suspended, the wavelength may depend on the size of the pattern.[48] In the latter case, the wavelength λ of generated wrinkles is correlated to the thickness of the Nafion film t, Poisson's ratio ν, strain ε, and pattern size L, as

$$\lambda = \frac{(2\pi t L)^{1/2}}{[3(1-\nu^2)\varepsilon]^{1/4}} \tag{2}$$

In our experiment, as the film thickness (t = 25.4 μm), the Poisson's ratio (ν = 0.4), and the strain (ε = 0.07 at 23 °C, water absorption) were constant, the L dependence of λ could be well compared to the prediction as

$$\lambda \approx 250 \left(\frac{L}{500}\right)^{1/2} \tag{3}$$

The comparison is important to determine how weakly the film interacts with the substrate and whether the wavelength of the wrinkles is proportional to $L^{1/2}$ in the case of weak interaction. Within each pattern shape, the theoretical and measured wavelengths are compared in Figure S7. All errors were within 10%, and it was confirmed that the wavelength was
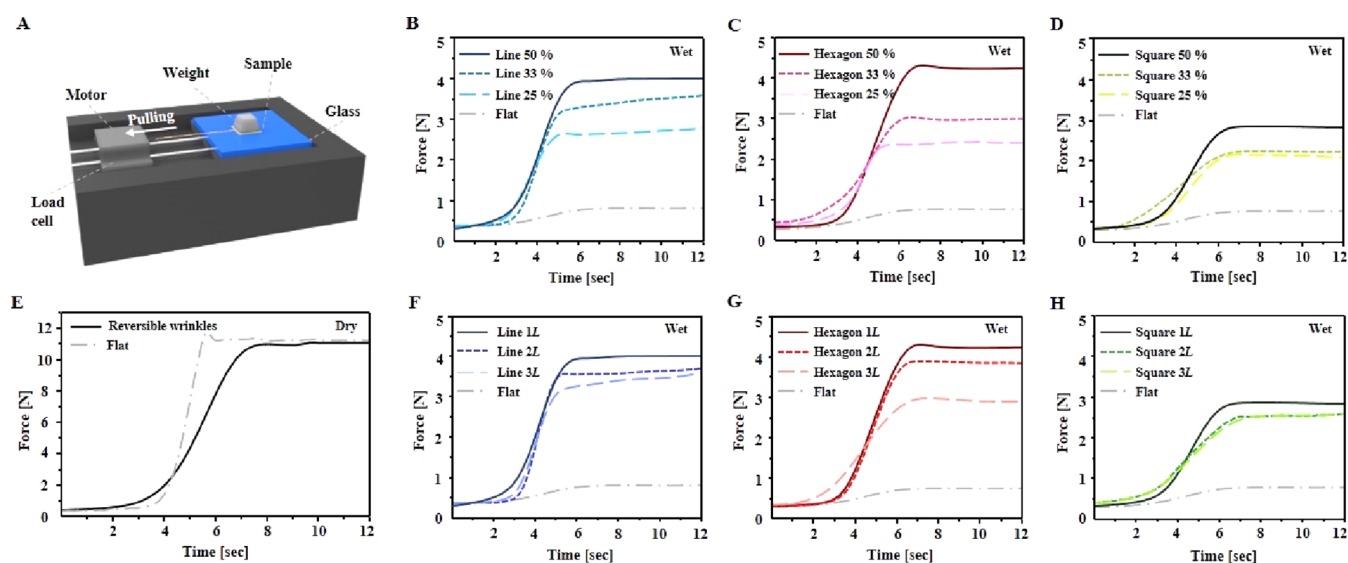
Figure 4. Comparison of frictional forces among different reversible wrinkle-inspired samples in wet and dry conditions. (A) Schematic illustration of the experimental set-up for friction measurement. (B−H) Frictional force of diverse samples in wet (B−D, F−H) and dry (E) states measured with a 200 g weight. All gray lines indicate the friction of a control sample with a flat surface that does not generate any wrinkles in wet and dry environments. (B−D) Frictional force of samples with different percentages of the patterned area (50, 33, and 25%), following the shapes of line (B), hexagon (C), and square (D). (E) Friction of reversible wrinkle-resembling samples and the control sample in dry conditions. (F−H) Frictional force of samples with different pattern sizes (1L, 2L, and 3L) following the shapes of line (F), hexagon (G), and square (H).

proportional to the square root of size L. This tendency also corresponded well with the contact area ratio (Figure 3D). Although delamination is not considered, the pattern size-wavelength equation makes a good fit to experimental data. This means that even when wrinkles are formed in the telephone cord mode by the large pattern, the compressive stress induced by the pattern shape mainly acts on the wavelength of the wrinkle. However, there is a slight deviation within the same pattern size, as shown in Table S3. The average wavelength of the wrinkles was smaller for the hexagonal pattern, followed by line and square patterns, respectively. It means that the Nafion film weakly interacts with the substrate (PDMS) in our system, but eq 2 is a uniaxial strain simplification of a real situation of complex shape patterns, which can be understood as a simple estimation. Lastly, to confirm the wrinkling of the Nafion film, the cross-section of the sample during the formation of the wrinkle was observed (Figure S8). Wrinkles appeared on the surfaces, which then resulted in an empty space between PDMS and the film. Also, we observed the wrinkle development and extinction with fast response times of less than 0.4 s per cycle, which was similar to the FEM results (Figure S9). As the extinction of wrinkles is relevant to the evaporation of water, the response time of the wrinkle disappearance by blowing high-temperature air (80 °C) was faster than that by blowing room-temperature air (23 °C). Since humidity is also a relevant factor in water evaporation, lower relative humidity (RH) induced faster extinction of wrinkles, which was between 0.19 and 0.76 s, depending on RH. When blowing room-temperature air for 15 cycles at an RH of 80% and at 23 °C, average response times of wrinkle generation and disappearance are 0.12 and 0.20 s, respectively (Figure S10).

2.4. Measurement of Frictional Forces of Various Patterned Surfaces. Based on the study of wrinkles, a multifunction adhesion tester was used for an accurate measurement of frictional force in each case (Figure 4A). The value of friction was obtained by strain gauges of a load

cell, as a sample under the weight (200 g) was pulled using a motor at a constant speed. The force under different weights (100, 50, and 10 g) was also measured, and the changes in real wrinkling morphologies and contact area ratios under the variety of weights were investigated (Figure S11). Each force of the samples with different pattern densities and pattern shapes was measured on wet surfaces (Figure 4B−D). Because frictional force is proportional to the contact area, the measured frictional force was proportional to the contact area ratios in Figure 3b. Similar to the tendency of contact area ratios, the measured frictional force was also proportional to pattern densities. Next, in the same way, the friction measurement results of the samples with different pattern shapes and sizes were obtained (Figure 4F−H). In the case of the line pattern, the length effect was investigated, but the results showed little change according to the length change (Figure S12). These results coincided with the tendency of contact area ratios in Figure 3D. Frictional force was inversely proportional to the root of size L. In addition, when the pattern density was 50%, the frictional force was higher in the following order of hexagonal, line, and square patterns, while it was in the order of line, hexagonal, and square patterns in other percentages of 33 and 25%. All of the frictional forces of the wrinkled samples were higher than those of the control sample (gray line) with flat surfaces because the crests and troughs of wrinkles prevented the hydroplaning phenomenon by creating channels to drain water. On the same principle, enhanced friction was obtained even under water, which provided a result similar to that of the friction on moisturized surfaces (Figure S13). In dry environments, our samples had a similar frictional force to the control sample (Figure 4E). Additionally, the dynamic process of wrinkle formation and disappearance could be cycled at least 5000 times without frictional change and other damage, demonstrating the robustness of our systems (Figure S14) and that the reversible wrinkling surfaces could be continuously sustained for more than 1 month in water (Figure S15).
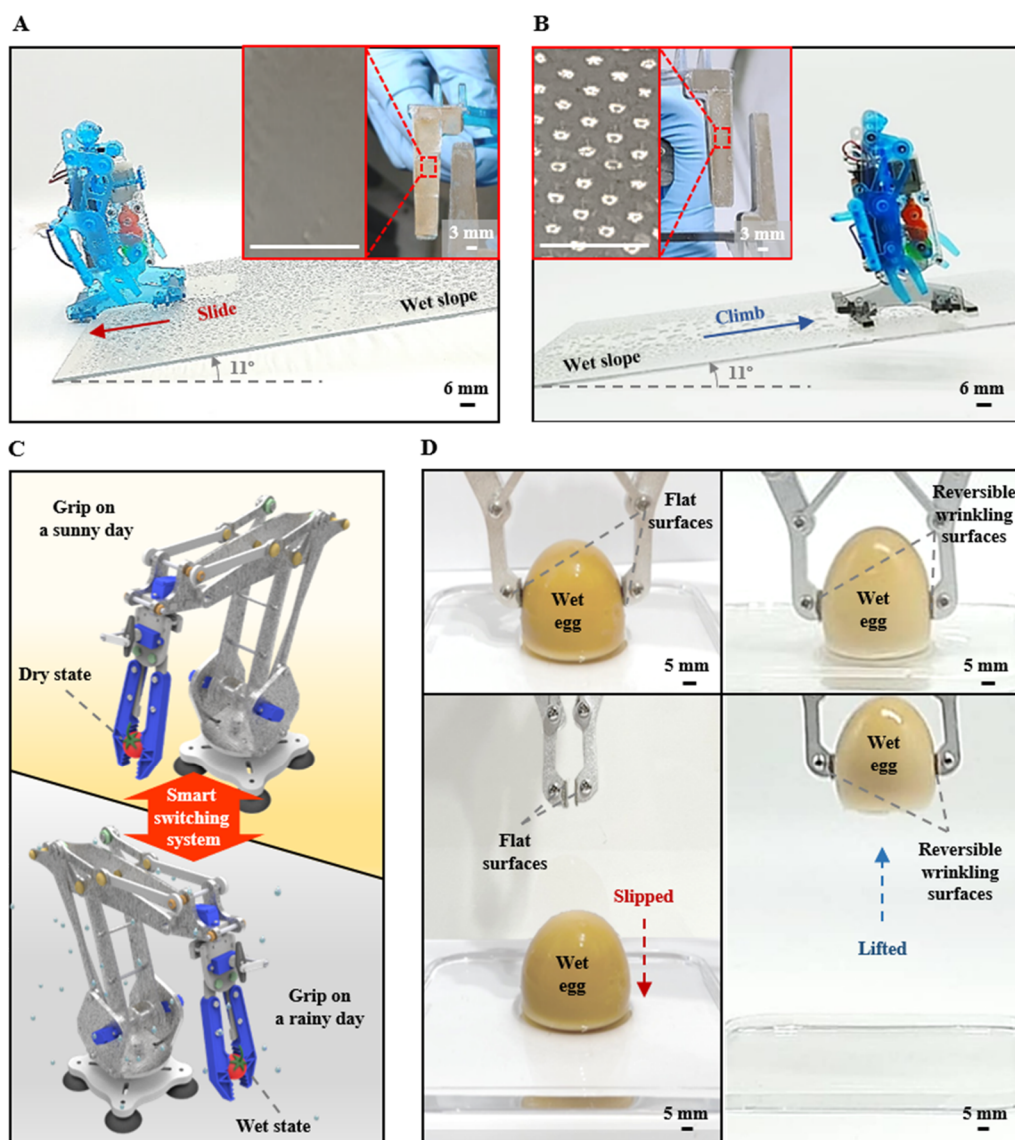
Figure 5. Applications of reversible wrinkles to walking robots and grippers of agricultural product-picking robots, which require high friction in wet and dry conditions. (A) Robot with flat feet that failed to climb the wet slope. (B) Robot with reversible wrinkled structures (hexagon 1*L*, 50%) on its feet. It manages to ascend the steep and wet surface without slipping. (C) Schematic illustration of an agricultural product-picking robot with our smart switching system applied to its gripper, which can help pick up fruits on sunny and rainy days. (D) Comparison between the gripper with the flat-surface control samples (left) and the gripper with the reversibly wrinkled structures (hexagon 1*L*, 50%, right), both of which lifted a wet egg.

As boundary conditions in a specific pattern induce symmetric wrinkles, one may expect that frictional force depends on an angle. To study the angle effect of the pattern shape on frictional force, the frictional force of each pattern shape was measured by changing the motion direction from 0 to 180°. As seen in Figure S16, the force changes with a clear sinusoidal cycle. The force was maximum when the sample moved along the crests of the wrinkles and was minimum when it moved across the crests of them. The periodicity of the experimental data was analyzed by Fourier transformation (Figure S16, lower row), and a sinusoidal fitting graph was derived by

$$\text{force} = A + B \sin\left[2\pi\left(\frac{\theta - C}{T}\right)\right] \tag{4}$$

where θ is the angle of motion; T is the period; *and* A, B, and C are constants. The obtained frequency from the experiment data matched well with the period of the fitted graph. As expected, the line pattern shows two extreme values (one minimum and one maximum) in the 180° range, and its period is 180°(=180°/1); hexagon one shows six extreme values (three minimum and three maximum) in the range, and the period is 60° (=180°/3); square one shows four extreme values (two minimum and two maximum) in the range, and the period is 90° (=180°/2). These results exactly matched the symmetry of the pattern features. Among the three shapes, the hexagon developed the most independent wrinkles in the movement direction where the period is the shortest and the change in the rate of the frictional force is the least.

Within the same-sized pattern and patterned area, lines and hexagons generated a larger force than squares, as in the above analysis. However, due to the difficulty in controlling the

direction of the system movement and lines, the hexagonal pattern is suitable for various industrial fields.

In general, it was found that the measured friction forces tend to be the same as a result of the contact area ratio analyzed in Figure 3. The smaller the wavelength is, the larger the contact area ratio becomes. This then results in larger friction on wet surfaces. Also, the wrinkles in the hexagonal pattern show less angular dependence of frictional force than those in other shapes. Therefore, 50% of $1L$ sized hexagonal patterns were the most suitable for our purpose.

2.5. Applications of Reversible Wrinkling Surfaces.
To demonstrate the ability of our smart structures in generating a large frictional force in both wet and dry conditions, a walking robot with our samples (hexagonal, 50%, $1L$) attached to the feet was made to climb on a slope (slope angle of 11°). Compared to a robot with flat feet, the robot with wrinkled feet did not slip and mounted well on a wet slope (Figure 5A,B). On a dry slope, both robots had flat feet and ascended well (Figure S17 and Movie S2). This shows that our reversible wrinkled structure can provide a solution to overcome the limitations of robots performing with or without the presence of water.

Figure 5C presents another example of how our devices are applied to an agricultural product-picking robot. The robot with smart switching systems helps to pick up fruits successfully not only on sunny days but also on rainy days without slipping and scratching. To verify the applicability of the harvesting robot, the grippers with our smart structures and with stable wrinkled surfaces were prepared to lift a dry egg. Compared to the gripper with the stable wrinkled surfaces, the gripper with our structures raised the egg well, although a small force (1 N) was applied on the gripper (Figure S18). This result shows that devices with our smart structures can achieve low energy consumption and verifies the requirement of flat surfaces in dry states. Next, with the flat-surface control samples, the gripper can hold a dry egg (Figure S19 left) but not a wet egg (Figure 5D left). However, the gripper with our samples (hexagonal, 50%, $1L$) successfully lifted an egg, wet (Figure 5D right) or dry (Figure S19 right). The force exerted by the gripper was 2 N, and there was negligible deformation of the egg while lifting it (Movie S3).

3. CONCLUSIONS
We have successfully demonstrated that our smart system, inspired by reversible wrinkles in a human finger, improves friction in both dry and wet environments. These structures could be fabricated with the Nafion membrane, and diverse morphologies of the wrinkles could be generated on the film by various micro-patterned PDMS (three different pattern sizes, shapes, and densities). By changing these factors, we studied the relationship between wrinkles and friction in each case, and we confirmed that a smaller-sized hexagonal pattern with a higher density generated a higher frictional force. Based on this finding, our reversible wrinkling system was applied to a robot that needs to walk on wet and dry slopped surfaces and a gripper that has to lift up a dry or wet egg. This shows that our smart switching system boasts high applicability to a variety of robots including those that are required to function in and out of water in the near future.

4. EXPERIMENTAL SECTION
4.1. Fabrication of Reversible Wrinkling Surfaces.
PDMS molds were prepared by replica molding from silicon masters

fabricated by conventional photolithography. A mixture of base and curing agents (10:1 w/w, Sylgard 184 polydimethyl siloxane elastomer) was poured onto the patterned masters and cured in an oven at 70 °C for 2 h. The cured molds were demolded from the masters and cut properly for use. On the molds, self-assembled monolayers were treated (SAM treatment) by using tricholoro ($1H,1H,2H,2H$-perfluorooctyl) silane (20 μL, Sigma-Aldrich) at a vacuum desiccator for 15 min. The second PDMS molds were obtained by imprint lithography. The treated molds were placed on a small amount of the PDMS mixture, which was the same as the one used above (10:1 w/w). Under a small pressure, they were hardened at 70 °C for 2 h. Through oxygen plasma-assisted bonding, these solidified samples were attached to a flexible PET film (50 μm), which was coated with an adhesion primer (Minuta Tech, South Korea). The second PDMS molds bonded with the film were peeled off from SAM-treated molds. Nafion (DuPont Nafion PFSA membrane NRE-211 (25.4 μm) purchased from CNL energy, South Korea) was placed on the second mold, and then UV-curable prepolymers, NOA (Norland Optical Adhesive 61 purchased from INEXUS INC. 4science, South Korea), were dropped between the Nafion and PDMS molds for a capillary action. These samples were exposed to UV light for 15 min and trimmed.

4.2. Fabrication of Control Samples.
The primer-coated PET film (50 μm) was attached to the cured PDMS (10:1 w/w, Sylgard 184 PDMS elastomer), whose surface was flat without patterning through oxygen plasma-assisted bonding. The UV-curable prepolymers (NOA 61) were dropped on the PDMS, and then Nafion (Nafion 211, 25.4 μm) was placed on the NOA. Having been pressed lightly, the sample was cured by UV exposure for 15 min and then trimmed.

4.3. Fabrication of Samples with Stable Wrinkled Surfaces.
The sample (hexagon $1L$ 50%) in water was frozen rapidly with liquid nitrogen, and then an UV-curable polymer, polyurethane acrylate (PUA 301, Sigma-Aldrich), was poured on the frozen samples and cured under ultraviolet (UV). On the cured polymer, SAM treatment was conducted by using tricholoro ($1H,1H,2H,2H$-perfluorooctyl) silane (20 μL, Sigma-Aldrich) at a vacuum desiccator for 15 min. Using the SAM-treated polymer as a master mold, the UV curing process with PUA was repeated one more time, and the replica was finally obtained. Then, spin coating of Nafion (5 wt % in lower aliphatic alcohols and water, Sigma-Aldrich) was conducted on the replica that retained the wrinkling surfaces of the sample.

4.4. Measurement Method.
Optical images were seen using an optical microscope (Omano OM2344, China). Optical microscopic images of the cross-section of samples were obtained using an optical microscope (Olympus IX70, Japan). Development and extinction of wrinkles were observed using an optical microscope (Olympus BX51, Japan) with a scan-speed camera (XTCam-D310CM, Japan, 1000 frames per second). In the observation of wrinkle disappearance, a heat gun (D26414, DeWalt) and a rubber blower (EXB-600, EXSO) were used to induce evaporation of water. Also, the effect of humidity on wrinkle extinction times was observed in the custom-built humidity control chamber, which includes the water atomizer and humidity sensor. Features of wrinkles in terms of contact area ratios and wavelengths were analyzed using a Java-based image-processing program, ImageJ, in the optical microscopic images using 2% aqueous solution of polystyrene micro-particles (micro particle size standard based on PS monodisperse 1.0 μm, Sigma-Aldrich). The wavelengths were measured as the length between two successive crests or troughs of the wrinkles. Amplitudes of wrinkles were measured using a surface profiler (ET200, KOSAKA). Three-dimensional profiles of the wrinkling surfaces were obtained using a confocal laser scanning microscope (LSM 800 MAT, Carl Zeiss). As LSM measurement is difficult in water, replica samples that retain wrinkling surfaces in dry conditions were prepared. The replicas were fabricated by the same method as mentioned in the fabrication of samples with stable wrinkled surfaces. Frictional forces were measured using a multifunctional adhesion tester (FCMS 170 was purchased from Neoplus Inc., South Korea).

4.5. FEM Analysis. For the study on the wrinkling mechanism and wrinkle morphologies, the finite element method (FEM) was performed using a commercial FEM program (ABAQUS). In FEM-based numerical analysis for the wrinkling mechanism of the thin Nafion film, two mechanical factors, an adhesion to a substrate and a hygral expansion in the moisture environment, are considered. The adhesion is implemented by the built-in mixed-mode traction-separation model and a contact algorithm in ABAQUS. The moisture-stimulated expansion characteristic is effectively implemented by the means of the numerically equivalent combination of thermal expansion and temperature. Also, for the consideration of geometric non-linearity and dynamic factors, a quasi-static dynamic solver is harnessed. In this FE analysis, the S4R element is selected and its density of size is about ∼30 μm.

4.6. Climbing Test. Two types of walking robots were prepared. One was equipped with flat feet, whose surface consisted of control samples, and the other had feet with our smart switching systems. All the components were the same except for the feet. To see if they could climb or not in dry and wet environments, 11° sloped glass was used while spraying water made the sloped surface moist.

4.7. Gripping Test. Three grippers with stable wrinkled surface samples, flat-surface control samples, and our attached smart structures were prepared. They tried to hold a normal egg and a water-soaked egg. A constant 1 or 2 N force was applied using the stepping motor (Casun, 42SHD0024-20A) when they caught the egg.

■ ASSOCIATED CONTENT

ⓢ Supporting Information

The Supporting Information is available free of charge at https://pubs.acs.org/doi/10.1021/acsami.2c15653.

Nafion structure, numerical analysis of the wrinkle-generation process, the contact area measurement method, LSM images of the wrinkling surfaces, analysis of wavelength following pattern sizes, the cross-section image of the reversible wrinkling system, optical images of the dynamic wrinkling cycle, response time, analysis of friction with various weights in wet conditions, length effect of the line pattern, friction under water, durability test, stability test of wrinkling surfaces, angular dependence analysis, application (walking robot and gripper) in dry conditions, model parameters and material properties for the numerical analysis, and average wrinkle wavelengths (PDF).

Simulated evolution of wrinkles on various patterns (MP4),

climbing tests with a walking robot (MP4), and gripping tests (MP4)

■ AUTHOR INFORMATION

Corresponding Authors

Mansoo Choi − *Global Frontier Center for Multiscale Energy Systems and Department of Mechanical and Aerospace Engineering, Seoul National University, Seoul 08826, Korea;* ⓞ orcid.org/0000-0003-3198-6899; Email: mchoi@snu.ac.kr

Yong Whan Choi − *Division of Mechanical Convergence Engineering, College of MICT Convergence Engineering, Silla University, Busan 46958, Korea;* ⓞ orcid.org/0000-0003-1765-6877; Email: ccs08745@silla.ac.kr

Authors

Jooyeon Shin − *Global Frontier Center for Multiscale Energy Systems and Department of Mechanical and Aerospace Engineering, Seoul National University, Seoul 08826, Korea;* ⓞ orcid.org/0000-0002-4987-1865

Jong-Gu Lee − *Department of Mechanical and Aerospace Engineering, Seoul National University, Seoul 08826, Korea*

Gunhee Lee − *Department of Environment Machinery, Korea Institute of Machinery & Materials, Daejeon 34103, Korea*

Peter V. Pikhitsa − *Global Frontier Center for Multiscale Energy Systems, Seoul National University, Seoul 08826, Korea*

Sang Moon Kim − *Department of Mechanical Engineering, Incheon National University, Incheon 22012, Korea;* ⓞ orcid.org/0000-0002-2311-2211

Complete contact information is available at:
https://pubs.acs.org/10.1021/acsami.2c15653

Author Contributions

The manuscript was written through contributions of all authors. All authors have given approval to the final version of the manuscript.

Notes

The authors declare no competing financial interest.

■ ACKNOWLEDGMENTS

■ ABBREVIATIO

PET, polyethylene terephthalate
PDMS, polydimethylsiloxane
NOA, Norland optical adhesives
PTFE, polytetrafluoroethylene
PFA, perfluoroalkyl ether
FEM, finite element method
RH, relative humidity
LSM, a confocal laser scanning microscope

■ REFERENCES

(1) Jiang, H.; Hawkes, E. W.; Fuller, C.; Estrada, M. A.; Suresh, S. A.; Abcouwer, N.; Han, A. K.; Wang, S.; Ploch, C. J.; Parness, A.; Cutkosky, MR A Robotic Device Using Gecko-Inspired Adhesives Can Grasp and Manipulate Large Objects in Microgravity. *Sci. Robot.* **2017**, *2*, No. eaan4545.

(2) Li, S.; Stampfli, J. J.; Xu, H. J.; Malkin, E.; Diaz, E. V.; Rus, D.; Wood, R. J.A Vacuum-Driven Origami "Magic-Ball" Soft Gripper. *2019 International Conference on Robotics and Automation (ICRA)*; IEEE, 2019; pp 7401−7408.

(3) Linghu, C.; Zhang, S.; Wang, C.; Yu, K.; Li, C.; Zeng, Y.; Zhu, H.; Jin, X.; You, Z.; Song, J. Universal SMP Gripper with Massive and Selective Capabilities for Multiscaled, Arbitrarily Shaped Objects. *Sci. Adv.* **2020**, *6*, No. eaay5120.

(4) Ma, Y.; Ma, S.; Yang, W.; Yu, B.; Pei, X.; Zhou, F.; Liu, W. Sundew-Inspired Simultaneous Actuation and Adhesion/Friction Control for Reversibly Capturing Objects Underwater. *Adv. Mater. Technol.* **2019**, *4*, 1800467.

(5) Tian, H.; Li, X.; Shao, J.; Wang, C.; Wang, Y.; Tian, Y.; Liu, H. Gecko-Effect Inspired Soft Gripper with High and Switchable Adhesion for Rough Surfaces. *Adv. Mater. Interfaces* **2019**, *6*, 1900875.

(6) Wang, Y.; Yang, X.; Chen, Y.; Wainwright, D. K.; Kenaley, C. P.; Gong, Z.; Liu, Z.; Liu, H.; Guan, J.; Wang, T.; Weaver, J. C.; Wood, R. J.; Wen, L. A Biorobotic Adhesive Disc for Underwater Hitchhiking Inspired by the Remora Suckerfish. *Sci. Robot.* **2017**, *2*, No. eaan8072.

(7) Banerjee, H.; Kakde, S.; Ren, H.Orumbot: Origami-Based Deformable Robot Inspired by an Umbrella Structure. *2018 IEEE International Conference on Robotics and Biomimetics (ROBIO)*; IEEE, 2018; pp 910−915.

(8) Lee, D.-Y.; Kim, J.-K.; Sohn, C.-Y.; Heo, J.-M.; Cho, K.-J. High−Load Capacity Origami Transformable Wheel. *Sci. Robot.* **2021**, *6*, No. eabe0201.

(9) Bell, M. A.; Pestovski, I.; Scott, W.; Kumar, K.; Jawed, M. K.; Paley, D. A.; Majidi, C.; Weaver, J. C.; Wood, R. J. Echinoderm-Inspired Tube Feet for Robust Robot Locomotion and Adhesion. *IEEE Robot. Autom. Lett.* **2018**, *3*, 2222−2228.

(10) Ma, Y.; Ma, S.; Wu, Y.; Pei, X.; Gorb, S. N.; Wang, Z.; Liu, W.; Zhou, F. Remote Control over Underwater Dynamic Attachment/ Detachment and Locomotion. *Adv. Mater.* **2018**, *30*, 1801595.

(11) Baik, S.; Kim, Y.; Park, T.-J.; Lee, S. H.; Ho Bhang, C.; Pang, C. A Wet-Tolerant Adhesive Patch Inspired by Protuberances in Suction Cups of Octopi. *Nature* **2017**, *546*, 396−400.

(12) Choi, J.; Ghaffari, R.; Baker, L. B.; Rogers, J. A. Skin-Interfaced Systems for Sweat Collection and Analytics. *Sci. Adv.* **2018**, *4*, No. eaar3921.

(13) Yang, Q.; Wei, T.; Yin, R. T.; Wu, M.; Xu, Y.; Koo, J.; Choi, Y. S.; Xie, Z.; Chen, S. W.; Kandela, I.; Yao, S.; Deng, Y.; Avila, R.; Liu, T.-L.; Bai, W.; Yang, Y.; Han, M.; Zhang, Q.; Haney, C. R.; Benjamin Lee, K.; Aras, K.; Wang, T.; Seo, M.-H.; Luan, H.; Lee, S. M.; Brikha, A.; Ghoreishi-Haack, N.; Tran, L.; Stepien, I.; Aird, F.; Waters, E. A.; Yu, X.; Banks, A.; Trachiotis, G. D.; Torkelson, J. M.; Huang, Y.; Kozorovitskiy, Y.; Efimov, I. R.; Rogers, J. A. Photocurable Bioresorbable Adhesives as Functional Interfaces between Flexible Bioelectronic Devices and Soft Biological Tissues. *Nat. Mater.* **2021**, *20*, 1559−1570.

(14) Xiao, Y. Y.; Jiang, Z. C.; Tong, X.; Zhao, Y. Biomimetic Locomotion of Electrically Powered "Janus" Soft Robots Using a Liquid Crystal Polymer. *Adv. Mater.* **2019**, *31*, 1903452.

(15) Fang, M.; Liu, T.; Xu, Y.; Jin, B.; Zheng, N.; Zhang, Y.; Zhao, Q.; Jia, Z.; Xie, T. Ultrafast Digital Fabrication of Designable Architectured Liquid Crystalline Elastomer. *Adv. Mater.* **2021**, *33*, 2105597.

(16) Jiao, Z.; Ji, C.; Zou, J.; Yang, H.; Pan, M. Vacuum-Powered Soft Pneumatic Twisting Actuators to Empower New Capabilities for Soft Robots. *Adv. Mater. Technol.* **2019**, *4*, 1800429.

(17) Mosadegh, B.; Polygerinos, P.; Keplinger, C.; Wennstedt, S.; Shepherd, R. F.; Gupta, U.; Shim, J.; Bertoldi, K.; Walsh, C. J.; Whitesides, G. M. Pneumatic Networks for Soft Robotics That Actuate Rapidly. *Adv. Funct. Mater.* **2014**, *24*, 2163−2170.

(18) Autumn, K.; Liang, Y. A.; Hsieh, S. T.; Zesch, W.; Chan, W. P.; Kenny, T. W.; Fearing, R.; Full, R. J. Adhesive Force of a Single Gecko Foot-Hair. *Nature* **2000**, *405*, 681−685.

(19) Geim, A. K.; Dubonos, S.; Grigorieva, I.; Novoselov, K.; Zhukov, A.; Shapoval, S. Y. Microfabricated Adhesive Mimicking Gecko Foot-Hair. *Nat. Mater.* **2003**, *2*, 461−463.

(20) Iturri, J.; Xue, L.; Kappl, M.; García-Fernández, L.; Barnes, W. J. P.; Butt, H. J.; del Campo, A. Torrent Frog-Inspired Adhesives: Attachment to Flooded Surfaces. *Adv. Funct. Mater.* **2015**, *25*, 1499−1505.

(21) Drotlef, D. M.; Stepien, L.; Kappl, M.; Barnes, W. J. P.; Butt, H. J.; del Campo, A. Insights into the Adhesive Mechanisms of Tree Frogs Using Artificial Mimics. *Adv. Funct. Mater.* **2013**, *23*, 1137−1146.

(22) Federle, W.; Barnes, W.; Baumgartner, W.; Drechsler, P.; Smith, J. Wet but not Slippery: Boundary Friction in Tree Frog Adhesive Toe Pads. *J. R. Soc. Interface* **2006**, *3*, 689−697.

(23) Emerson, S. B.; Diehl, D. Toe Pad Morphology and Mechanisms of Sticking in Frogs. *Biol. J. Linn. Soc.* **1980**, *13*, 199−216.

(24) Savkoor, A. Some Aspects of Friction and Wear of Tyres Arising From Deformations, Slip and Stresses at the Ground Contact. *Wear* **1966**, *9*, 66−78.

(25) Huber, G.; Mantz, H.; Spolenak, R.; Mecke, K.; Jacobs, K.; Gorb, S. N.; Arzt, E. Evidence for Capillarity Contributions to Gecko Adhesion from Single Spatula Nanomechanical Measurements. *Proc. Natl. Acad. Sci. U.S.A.* **2005**, *102*, 16293−16296.

(26) Clark, C. V.; Pentland, B.; Ewing, D. J.; Clarke, B. F. Decreased Skin Wrinkling in Diabetes Mellitus. *Diabetes Care* **1984**, *7*, 224−227.

(27) Braham, J.; Sadeh, M.; Sarova-Pinhas, I. Skin Wrinkling on Immersion of Hands: a Test of Sympathetic Function. *Arch. Neurol.* **1979**, *36*, 113−114.

(28) O'Riain, S. New and Simple Test of Nerve Function in Hand. *Br. Med. J.* **1973**, *3*, 615−616.

(29) Kareklas, K.; Nettle, D.; Smulders, T. V. Water-Induced Finger Wrinkles Improve Handling of Wet Objects. *Biol. Lett.* **2013**, *9*, 20120999.

(30) Sun, Y.; Wu, K.; Wang, Y.; Zhang, J.; Liu, G.; Sun, J. Controlled Wrinkling Patterns and Surface Friction by Thickness Gradient. *Surf. Coat. Technol.* **2020**, *401*, 126279.

(31) Yuan, H.; Wu, K.; Zhang, J.; Wang, Y.; Liu, G.; Sun, J. Curvature-Controlled Wrinkling Surfaces for Friction. *Adv. Mater.* **2019**, *31*, 1900933.

(32) Rand, C. J.; Crosby, A. J. Friction of Soft Elastomeric Wrinkled Surfaces. *J. Appl. Phys.* **2009**, *106*, 064913.

(33) Yu, S.; Li, L.; Wang, J.; Liu, E.; Zhao, J.; Xu, F.; Cao, Y.; Lu, C. Light-Boosting Highly Sensitive Pressure Sensors Based on Bioinspired Multiscale Surface Structures. *Adv. Funct. Mater.* **2020**, *30*, 1907091.

(34) Li, L.; Zheng, Y.; Liu, E.; Zhao, X.; Yu, S.; Wang, J.; Han, X.; Xu, F.; Cao, Y.; Lu, C.; Gao, H. Stretchable and Ultrasensitive Strain Sensor Based on a Bilayer Wrinkle-Microcracking Mechanism. *Chem. Eng. J.* **2022**, *437*, 135399.

(35) Xu, F.; Fu, C.; Yang, Y. Water Affects Morphogenesis of Growing Aquatic Plant Leaves. *Phys. Rev. Lett.* **2020**, *124*, 038003.

(36) Mohammadi, H.; Müser, M. H. Friction of Wrinkles. *Phys. Rev. Lett.* **2010**, *105*, 224301.

(37) Kim, S. J.; Yoon, J.-I.; Moon, M.-W.; Lee, K.-R. Frictional Behavior on Wrinkle Patterns of Diamond-Like Carbon Films on Soft Polymer. *Diam. Relat. Mater.* **2012**, *23*, 61−65.

(38) Yu, S.; Guo, Y.; Li, H.; Lu, C.; Zhou, H.; Li, L. Tailoring Ordered Wrinkle Arrays for Tunable Surface Performances by Template-Modulated Gradient Films. *ACS Appl. Mater. Interfaces* **2022**, *14*, 11989−11998.

(39) Ma, T.; Bai, J.; Li, T.; Chen, S.; Ma, X.; Yin, J.; Jiang, X. Light-Driven Dynamic Surface Wrinkles for Adaptive Visible Camouflage. *Proc. Natl. Acad. Sci. U.S.A.* **2021**, *118*, No. e2114345118.

(40) Wu, K.; Sun, Y.; Yuan, H.; Zhang, J.; Liu, G.; Sun, J. Harnessing Dynamic Wrinkling Surfaces for Smart Displays. *Nano Lett.* **2020**, *20*, 4129−4135.

(41) Zhao, Q.; Majsztrik, P.; Benziger, J. Diffusion and Interfacial Transport of Water in Nafion. *J. Phys. Chem. B* **2011**, *115*, 2717−2727.

(42) Goswami, S.; Klaus, S.; Benziger, J. Wetting and Absorption of Water Drops on Nafion Films. *Langmuir* **2008**, *24*, 8627−8633.

(43) Mauritz, K. A.; Moore, R. B. State of Understanding of Nafion. *Chem. Rev.* **2004**, *104*, 4535−4586.

(44) Moon, M.-W.; Lee, K.-R.; Oh, K.-H.; Hutchinson, J. W. Buckle Delamination on Patterned Substrates. *Acta Mater.* **2004**, *52*, 3151−3159.

(45) Hutchinson, J. W.; Suo, Z. Mixed Mode Cracking in Layered Materials. *Adv. Appl. Mech.* **1991**, *29*, 63−191.

(46) Lin, H.-T.; Hong, T.-F.; Li, W.-L. Grip Performance Affected by Water-Induced Wrinkling of Fingers. *Tribol. Lett.* **2015**, *58*, 38.

(47) Chung, J. Y.; Nolte, A. J.; Stafford, C. M. Surface wrinkling: a versatile platform for measuring thin-film properties. *Adv. Mater.* **2011**, *23*, 349−368.

(48) Cerda, E.; Mahadevan, L. Geometry and Physics of Wrinkling. *Phys. Rev. Lett.* **2003**, *90*, 074302.